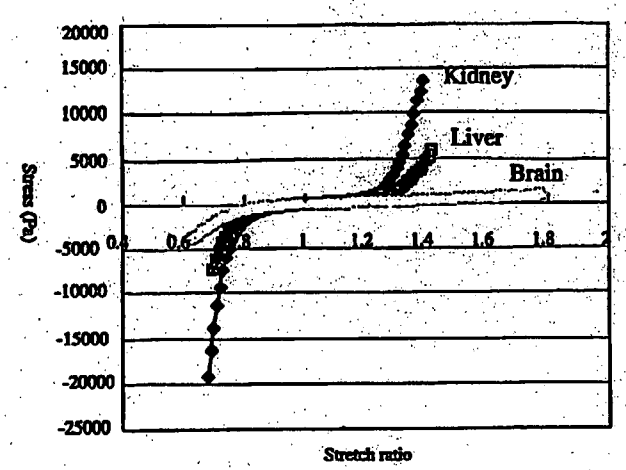

Fig. 6. Comparison of experimental stress–strain data from combined compression and elongation tests of liver, kidney and brain tissues: number of samples = 5 for each tissue type; diameter: 7 mm; loading rate: 10 mm/min.

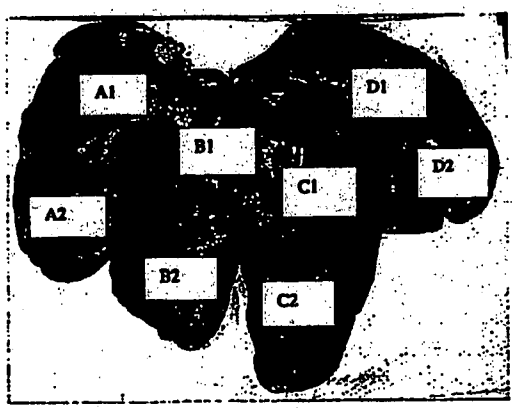

	Density (g/cm³)
A1	1.070
A2	1.078
B1	1.030
B2	1.074
C1	1.058
C2	1.074
D1	1.074
D2	1.057

Fig. 7. Mass densities of tissue samples extracted from different parts of the liver.

by dividing the measured weight by the volume of the tissue sample. There is no apparent different in the stress–strain relationship of these tissue samples in uniaxial loading tests.

From the comparison of the stress–strain curves from visceral side, diaphragmatic side and edge of the liver organs, it was observed that samples extracted from the upper surface (diaphragmatic side) of liver were noticeably harder than those from other parts of the liver. In the experiment,[25] a total of 21

samples were extracted from two porcine livers. Height of the cylindrical samples was about 5 mm. The loading rate was 10 mm/min. The presence of a thin capsular layer on the liver surface may help contribute to the stiffness. Since we were mainly interested in computer aided surgical simulation, with surgical devices such as needles approaching liver from the top, samples extracted from the diaphragmatic side of liver were used in our bio-mechanical analyses of liver properties.

3.3. *Effects of temperature*

The effect of temperature on the mechanical properties of liver is clinically important. Diseased liver organ is heated in RF ablation procedure, and cooled in cryosurgery for cancer cell destruction. Figure 8 compares the stress–strain behavior of liver tissue at different temperature (22°C, 37°C, 60°C and 80°C). The material behavior of liver tissue was essentially the same at 22°C and 37°C. At 60°C, the nonlinear shape of stress–strain curve remains although the tissue is softer. At 80°C, the liver tissue was heat-denatured. This agrees with the observation from Haemunerich *et al.*[30] that water loss from the samples was significant at temperature above 70°C. Haemunerich *et al.* reported an *in vitro* heating of liver samples using two electrodes. In our cooling experiments, we found that freezing has significant effects on the mechanical properties of porcine liver tissue. Chua *et al.*[31] reported an analytical study on the thermal effects of cryosurgery.

The temperature of tissue samples could be maintained with Ringer solution circulated at a constant rate during experiments. Ringer solution is a solution that is isotonic with blood. One liter of ringer solution contains 130 mEq of sodium ion, 109 mEq of choride ion, 28 mEq of lactate, 4 mEq of potassium ion and 3 mEq of calcium ion.

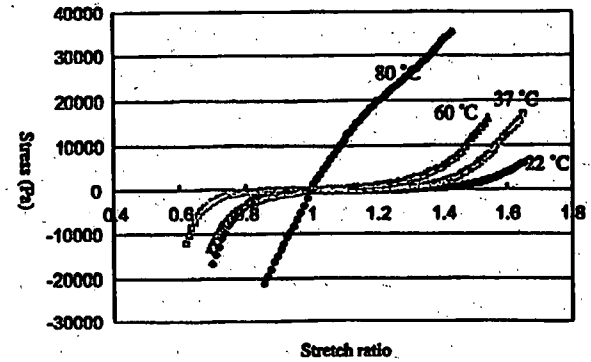

Fig. 8. Comparison of experimental stress–strain data from combined compression and elongation tests of liver tissues at different temperature: number of samples: 12 (3 at each temperature); diameter: 7 mm; loading rate: 10 mm/min.

3.4. *Strain rate dependency*

The effect of strain rate on porcine liver tissue was shown to be relatively insignificant from various experiments (e.g. Refs. 19 and 25). Constant speed of elongation/compression of 1, 2, 5, 10, 20, 50, 100 and 200 mm/min are corresponded to strain rates of 0.003, 0.006 0.030, 0.061, 0.151, 0.303 and 0.606 per second respectively. Varying strain rate has little effect on hysteresis from the stress–strain curves obtained from compression and then elongation testing. Hysteresis is the energy dissipation between the loading and unloading of the tissue during mechanical tests. Figure 9 shows the hysteresis measured during the cycle of compression and elongation to zero stress state in combined compression and elongation experiments with varying loading rates. There is little change in hysteresis when the loading rates range between 5 and 50 mm/min.

As was also reported for other animal tissues,[22] porcine liver exhibited tissue relaxation. During the relaxation experiments, the liver tissue sample was compressed, and then the compression was maintained, the amount of force measured gradually decreased.[26] At low loading rates (1–2 mm/min), some tissue relaxation was observed, while very fast rates (50–200 mm/min) resulted in large increments between data points. Liver tissue is not linear viscoelastic when the loading rates are between 5 and 50 mm/min. The loading rate of 10 mm/min was found to be the most suitable for extensive measurement experiments. This corresponded to a strain rate of between 0.041 per second and 0.015 per second since our samples ranged in height from 4 to 11 mm. This was consistent with values required for our targeted application, that is, computer aided surgical simulation for

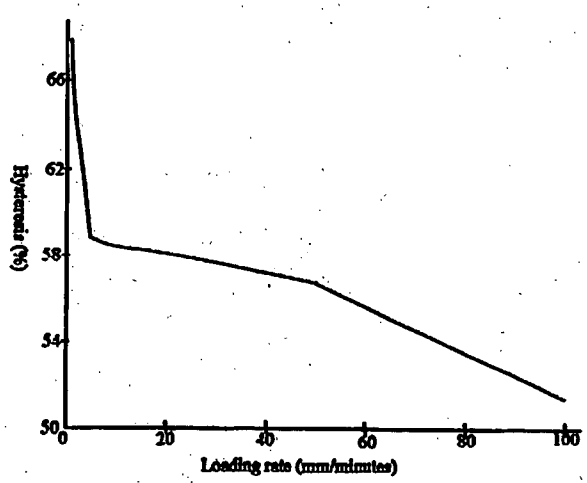

Fig. 9. Strain rate dependency of liver tissue sample: number of samples = 54 from 9 porcine livers; diameter and height of the samples were 7 mm and 5.5–10 mm respectively.

abdominal surgery. Slightly higher strain rates were included in our study because we needed to predict the initial response of liver to a surgical probe. By testing all samples at the same rate, confounding effects of tissue viscoelasticity could be minimized.

3.5. *Incompressibility and Poisson's ratio*

When a solid is subjected to load, it deforms and changes its shape and volume. The volume of an incompressible material remains constant when deform. Biological soft tissues including liver have often been assumed to be incompressible. Liver tissue incompressibility can be studied via measurement of Poisson's ratio. The values of Poisson's ratio for most engineering materials are constant and range between 0.25 and 0.35.

With reference to a cylindrical sample of height H and diameter D under a load τ, elastic elongation or compression in the direction of the applied load (known as axial strain ε_a) is accompanied by contraction or expansion in the perpendicular direction (known as transverse strain ε_t). Poisson's ratio is defined as the negative ratio of transverse strain to axial strain ($\varepsilon_t/\varepsilon_a$). Poisson's ratio is a material property that has received relatively less attention. This parameter is difficult to measure experimentally particularly for biological soft tissue which is generally heterogeneous and anisotropic, in addition to its softness which makes handling difficult.

To determine Poisson's ratio, a digital video camera was used to record the compression and elongation process with force at each instant measured and noted. The video was then processed, and broken into individual frames. Each frame was processed to determine the mean diameter of the tissue samples D, and this value was compared with the previous frame to determine ΔD. The Poisson's ratios during compression and elongation were readily determined since the axial displacement ΔH is known. Figure 10(a) illustrates the experimental setup used to determine the Poisson's ratio of liver tissue, and a typical frame captured using the digital camera was shown in Fig. 10(b).

In theory, Poisson's ratio for a biological material can vary from less than zero to over one half. This is in contrast to the 0–0.5 range for isotropic continua. Consistent with the theory, we have determined that the Poisson's ratio for compression and elongation were 0.466 ± 0.147 and 0.431 ± 0.155 respectively. The values were measured from a size of 15 tissue samples for compression and 24 tissue samples for elongation. Figure 11 compares the Poisson's ratio for compression and elongation.

3.6. *Anisotropy*

Markers on the test sample were prepared and deformation of the sample during experiment was recorded via a digital video camera described above. Figure 12 was snap shots in the middle and end of the tension experiment. We observed that

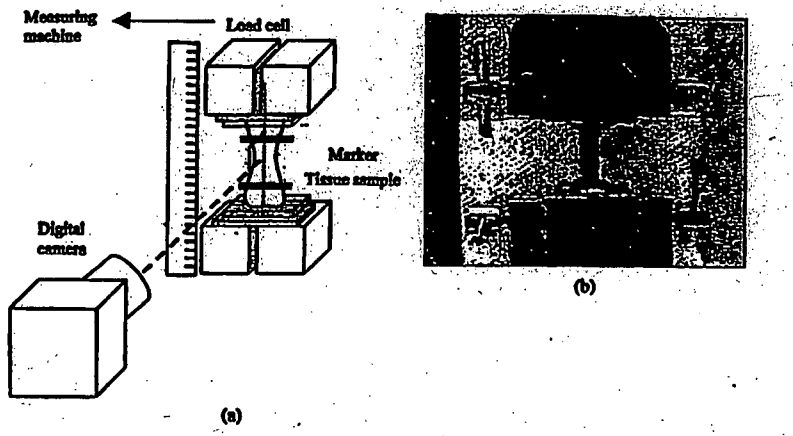

Fig. 10. Overview of experiments to determine Poisson's ratio of porcine liver tissues: (a) experimental setup for Poisson's ratio measurement; (b) snap shot of tissue sample during experiment.

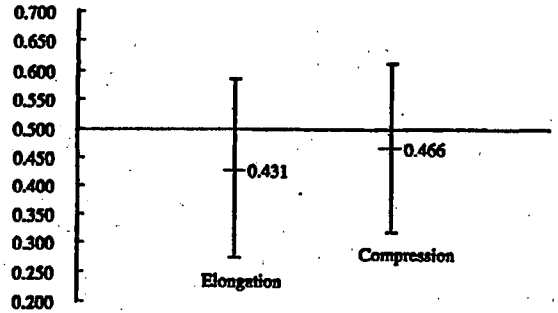

Fig. 11. Comparison of Poisson's ratio during elongation and compression experiments of liver tissue samples. Number of samples: 15 for compression; 24 for elongation.

there was a tendency for liver to displace in the direction of the force, which was acting perpendicular to the cross sectional x–y or horizontal plane. The originally horizontal marker placed on the specimen remained roughly horizontal at the middle and end of elongation. If there is no plane of symmetry or transverse, the marker will fail to remain horizontal. The horizontal displacement from necking differs from the vertical displacement. We did not observe any change in the shape of the cross sectional plane of the sample. The porcine liver tissue sample is likely to be a transversely isotropic material with the principal axis along the z direction or vertical plane. Investigation on the anisotropy properties of porcine liver tissue has been reported in Ref. 74.

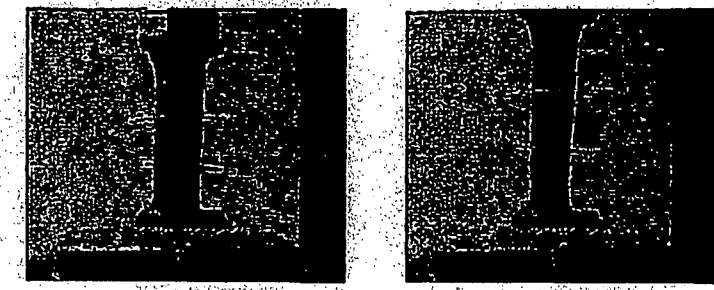

Fig. 12. Snap shots of deformation of liver tissue sample during experiment.

In summary, liver tissue is incompressible and is not isotropic at the length scale of approximately 10 mm. The liver tissue also possesses a nonlinear stress–strain behavior. It is not quite strain rate dependent. Linear viscoelasticity is not significant at moderate strain rate experienced during surgery. The liver tissue samples can be considered as a homogeneous material if they are extracted from the surface of the liver organ. They are noticeably harder than brain tissue and softer than kidney tissue.

4. Strength and Elastic Modulus of Liver Tissues

From investigation on the strength of liver tissue, the yield stress and strain were approximately 2.5×10^5 Pa and 69.5% for compression. With this yield stress, the compressive stress achieved by 1 N was one order of magnitude less than the yield stress. The resultant force–displacement relationship before and after preconditioning was found to have not change with 1 N of preconditioning load. Precondition may not be necessary since surgeon interacts with non preconditioned tissues and/or organ.

Assuming a linear elastic model, we determined that the mean modulus was 1355 kPa with a standard deviation of 0.7811×10^5 Pa. The mean yield stress was $-2.478 \pm 0.7811 \times 10^5$ Pa. The ultimate stress lies in the range of -1364×10^5 to -4.054×10^5 Pa. The maximum compression at rupture was between 61% and 79%. The measured parameters of the 13 *in vitro* destructive compression tests are listed in Table 1.

Determining Young's modulus of the liver tissue during elongation proved to be harder than compared with that of compression. This was due to our experimental method using surgical bond in attaching the specimen to the measuring instrument. As described in Sakuma *et al.*[26] this method had an advantage in stress concentration and possessed no slipping as in conventional uniaxial tests using clamps. However, the bond adhesiveness was weaker compared

Table 1. Material parameters measured from compression of liver specimens. The diameter and height of each specimen was 7 mm and 5 mm respectively. Stress is in terms of 1×10^5 N/m^2 and Young's modulus is in terms of 1×10^6 N/m.^{2}

Specimen	Yield		Maximum		Break		Young's modulus
	Stress	Strain (%)	Stress	Strain (%)	Stress	Strain (%)	
1	−3.118	−71	−3.352	−74	−3.066	−76	1.299
2	−3.637	−71	−3.767	−73	−3.611	−75	2.055
3	−3.118	−73	−3.507	−75	−3.170	−76	1.359
4	−2.910	−69	−3.144	−72	−2.858	−74	1.336
5	−1.948	−72	−2.104	−74	−1.974	−75	1.006
6	−2.468	−75	−2.754	−77	−2.442	−79	1.862
7	−1.922	−72	−2.130	−74	−1.689	−75	1.380
8	−2.546	−75	−2.754	−77	−2.598	−78	1.110
9	−2.468	−75	−2.754	−77	−2.442	−79	1.862
10	−3.637	−71	−4.053	−74	—	—	1.707
11	−1.546	−59	−1.689	−61	—	—	0.707
12	−1.533	−58	−1.611	−60.5	−1.585	−61	0.890
13	−1.351	−63	−1.364	−64	−1.039	−70	1.039
Mean	−2.478	−69.54	−2.691	−71.82	−2.313	−74.36	1.355
Standard deviation	0.781	5.825	0.862	5.988	0.805	5.104	0.413
Range	(−1.351, −3.638)	(58, 75)	(−1.364, −4.054)	(60.5, 77.4)	(−1.039, −3.612)	(61, 79)	(0.707, 2.055)

to the liver tissue. The attachment gave way prior to the break point of the liver tissue during elongation. In order to overcome this problem, separate tests using clamps were conducted to measure the ultimate stress and strain. The measured material parameters of all the seven tests are listed in Table 2. We determined that the mean value of ultimate stress and ultimate strain were 6.9×10^4 Pa and 79% respectively. Young's modulus was 227 kPa. This is significantly smaller than that determined during compression.

For comparison, liver tissue was stiffer than the muscular tissue and somewhat close to artery tissue. The artery tissue can withstand a larger strain compared to that of liver tissue. It was reported in the literature that Young's modulus, maximum stress and strain of artery were 200 kPa, 2×10^6 N/m^2 and 100% respectively during elongation. For muscular tissue, the corresponding values were 30 kPa, 2×10^5 N/m^2 and 60%.

Note that engineering stress and strain were referenced in the above discussions. For comparison, Young's modulus was measured from true stress and true strain during elongation experiments. The Young's modulus ranged from 500 to 750 kPa. This was consistent with the value of 650 kPa from experiments by Toyota Co, Japan reported in Chui *et al.*[31] It was typical for Young's modulus calculated from

Table 2. Material parameters measured from elongation of liver specimens. Height is between 7 and 9.5 mm, stress is in 1×10^4 N/m,^{2} and Young's modulus is in 1×10^5 N/m.^{2} All specimens have the same initial cross sectional area with diameter = 0.007 m.

Specimen	Yield		Maximum		Young's modulus
	Stress	Strain (%)	Stress	Strain (%)	
1	4.9	68.89	6.756	86.67	2.046
2	4.9	68.75	5.847	86.25	2.161
3	2.9	71.76	3.378	77.06	1.822
4	5.8	59.50	7.2	68.0	2.620
5	8.4	70.00	10.0	82.0	2.695
6	8.0	60.00	8.6	65.0	2.857
7	5.8	82.00	6.7	88.0	1.727
Mean	5.826	68.7	6.926	79.0	2.276
Standard deviation	1.89	7.61	2.088	9.32	0.448
Range	(2.91, 8.4)	(59.5, 82)	(3.378, 10.0)	(65.0, 88.0)	(1.727, 2.857)

true stress to be higher than that calculated using engineering stress. Nevertheless, the different was significant.

5. Mathematical Description of Liver Tissue Elasticity

A constitutive equation describes a physical property of a material. Its derivation should begin with empirical measurements. There are two alternatives for constitutive modeling: the continuum approach and the microstructure approach. With the first approach, the material is assumed to be a continuum. The relevant variables are identified, and these are related in a framework that ensures invariance under a change of frames. This was our approach in this paper.

One of the earliest reported mathematical/experimental treatments of biologic materials in the context of large deformation and modern continuum mechanics was that of Ticker and Sacks, 1964 and 1967, according to Vossoughi.[33] Since then, a number of constitutive models have appeared that described the passive material properties of both hard and soft tissues. However, few deal with abdominal tissues such as the liver. If the material is linear and the deformation is limited and infinitesimal, then a simple linear relationship derived according to Hooke's law might be sufficient to uniquely describe the stress-strain relationship. The formulation is not unique for a nonlinear material capable of undergoing large deformations. One constitutive model may well represent one type of soft tissue but not the others, or a model may well approximate a portion of the stress-strain curve, but not the entire space. The numerical complexity of these nonlinear functions is also an issue for interactive computing using currently available computer hardware and software.

In Carter *et al.*[13] and Davies *et al.*[18,34] the authors described biomechanical modeling with experimental indentations of animal abdominal organs, including liver. Their study assumed that the tissues were isotropic, homogeneous and incompressible. A nonlinear constitutive model based on a strain energy polynomial function was used in Miller[35] to model liver and kidney, using experimental results from *in vivo* experiments on Rhesus monkeys by Melvin *et al.*[36] The experiments approximated uniaxial compression under high strain rates typical for car crashes. These nonlinear models were numerically complex, and not suitable for fast medical simulation.

A well-known approach for studying nonlinear constitutive relations of bodies capable of finite deformation is to postulate that elasticity has the form of an elastic potential, or strain energy function, W. A number of constitutive models based on strain energy have already been proposed to describe the passive material properties of soft tissues. For solid biomechanics, most of the work has concentrated on blood vessels and myocardium. There are fewer reports of work on lung, skin, ligament, tendon, cartilage and bone tissue. Chui *et al.*[25] reports strain energy based constitutive relation that is derived from extensive measurements on liver tissue samples. There are also some recent reports on empirical expressions for fitting uniaxial tensile stress–strain relationship of soft tissue. These expressions are generally computational efficient and do not reduce to the form of strain energy. We tried to determine a constitutive equation that could fit the experimental data. The theoretical curve should follow the shape of the average curve with small standard error. Standard error is defined as root means square errors (RMSE), and is calculated from the difference between the theoretical estimate and the experimental measurement. To estimate the coefficients for the nonlinear functions, software for nonlinear least-square data fitting using the Gauss–Newton method could be used. Generally, models with few material parameters are preferred for the purpose of computational efficiency. Numerical stability of the parameters is desired for finite element computation. Depending on the specific applications, the constitutive model used is a trade off between computational accuracy and interactivity. Stress–strain graphs of compression, elongation and combined compression and elongation experiments can be found in Chui *et al.*[25]

5.1. *Empirical expressions*

The most popular expression that is not reduced to the form of strain energy is the exponential function by Tanaka and Fung.[37,38] Tanaka and Fung proposed a constitutive relation for soft tissue for simple uniaxial state of stress–strain as:

$$\sigma = (\sigma^* + \beta)e^{C_1(\lambda-\lambda^*)} - C_2$$

where σ and λ are the stress and stretch ratio, $\sigma*$ and $\lambda*$ corresponds to a point on the stress–strain curve, C_1 and C_2 are the material constants. A variant from

Fung[22] with an additional material constant is,

$$T = C_1 e^{C_2\lambda} - C_3$$

where T is the engineering stress, C_1, C_2 and C_3 are the material constants. The other empirical formulae proposed to fit experimental stress–strain data include Kenedi *et al.*[39] and Ridge and Wright.[40] The former with two material constants is,

$$T = C_1\lambda^{C_2-1} - \frac{1}{\lambda}.$$

The empirical formulae are simple. However, they are limited to a uniaxial state of stress–strain. These equations could model the stress–strain curve of elongation reasonably well. Generally, they do not fit the experimental data on compression of liver tissues well. All of these equations could not model the stress–strain curve from combined compression and elongation experiments. A more general multi-axial based formulation is preferred for medical simulation.

5.2. *Strain energy functions*

The strain energy for an elastic body is a function of the state of deformation. Let $\mathbf{X}$ denotes a point in the reference configuration. The current position of the point is denoted by $\mathbf{x}$, where $\mathbf{x}$ is a function of time. The gradient of $\mathbf{x}$ with respect to $\mathbf{X}$ is called the deformation gradient,

$$\mathbf{F} = \left(\frac{\partial \mathbf{x}}{\partial \mathbf{X}}\right)^T.$$

The right Cauchy–Green tensor, $\mathbf{C}$ is a measure of the strain the body experiences and is given by

$$\mathbf{C} = \mathbf{F}^T\mathbf{F}.$$

The constitutive assumption of nonlinear elasticity is that the stress tensor at point $\mathbf{x}$ depends only on the material and the deformation gradient at $\mathbf{x}$. If the mechanical properties do not depend explicitly on the particular point $\mathbf{x}$, the material is said to be homogeneous. The liver tissue is assumed to be homogeneous and incompressible in this investigation.

When a quantity is unchanged with a frame rotation, it is said to be invariant. From $\mathbf{C}$, which is a second order tensor, three scalar invariants can be formed by taking the trace of $\mathbf{C}$, $\mathbf{C}^2$ and $\mathbf{C}^3$. They are

$$I = \text{trace}(\mathbf{C}) = C_{ii},\ II = \text{trace}(\mathbf{C}^2) = C_{ij}C_{ji} \text{ and } III = \text{trace}(\mathbf{C}^3) = C_{ij}C_{jk}C_{ki}.$$

However, it is customary to use strain invariants

$$I_1 = I,\quad I_2 = \frac{1}{2}(I^2 - II) \quad \text{and} \quad I_3 = \frac{1}{6}(I^3 - 3I \cdot II + 2III) = \det(\mathbf{C}).$$

Assuming that liver tissue is isotropic, the strain energy function can be expressed as a function of the above strain invariants, $W(I_1, I_2, I_3)$. We denote λ_i as the principal values of $\mathbf{F}$ and I_i is a function of λ_i.

$$\mathbf{F} = \begin{pmatrix} \lambda_1 & & \\ & \lambda_2 & \\ & & \lambda_3 \end{pmatrix}$$

Since liver is known to comprise highly incompressible material, $\det \mathbf{F} = \lambda_1\lambda_2\lambda_3 = 1$. Under uniaxial deformation, the cross-sectional area of the cylindrical sample reduces by $1/\lambda$ when the height of the sample is increased by a factor of λ. By setting $\lambda = \lambda_3$, we have $\lambda_1 = \lambda_2 = \frac{1}{\sqrt{\lambda_3}}$. Invariants I_1, I_2 and I_3 under uniaxial deformation can be evaluated as $I_1 = \lambda^2 + 2/\lambda$, $I_2 = 2\lambda + 1/\lambda^2$ and $I_3 = 1$, respectively.

For an elastic material, the second Piola-Kirchhoff stress tensor $\mathbf{S}$ can be expressed in terms of strain energy W and Green–Lagrange strain tensor $\mathbf{E}$ as

$$\mathbf{S} = \frac{\partial W}{\partial \mathbf{E}} = 2\frac{\partial W}{\partial \mathbf{C}}.$$

The Cauchy stress σ is related to $\mathbf{S}$ by

$$\sigma = \frac{1}{J}\mathbf{F}\cdot\mathbf{S}\cdot\mathbf{F}^T$$

where $J = \det \mathbf{F}$. Component of σ in the tensile or compressive direction could now be expressed as partial derivative of W by the invariants.

$$\sigma = 2\frac{\partial W}{\partial I_1}\left(\lambda^2 - \frac{1}{\lambda}\right) + 2\frac{\partial W}{\partial I_2}\left(\lambda - \frac{1}{\lambda^2}\right). \tag{1}$$

Cauchy stress σ is related to the first Piola-Kirchhoff stress tensor $\mathbf{T}$ by

$$\sigma = \frac{1}{J}\mathbf{F}\cdot\mathbf{T}.$$

Since $\sigma = \lambda T$, we can deduce from Eq. (1) that

$$T = \frac{2}{\lambda}\frac{\partial W}{\partial I_1}\left(\lambda^2 - \frac{1}{\lambda}\right) + \frac{2}{\lambda}\frac{\partial W}{\partial I_2}\left(\lambda - \frac{1}{\lambda^2}\right). \tag{2}$$

Suppose that the original cross sectional area of the cylindrical sample used in our experiment is A_0 and the tensile or compressive load is F,

$$T = \frac{F}{A_0}.$$

Suppose that the original length of the cylindrical sample is L_0, the displacement is $\Delta L = L_0(\lambda - 1)$.

T and ΔL are concurrently measured in the experiments. By comparing the experimental curve obtained by plotting T against λ with the theoretical curve from Eq. (2) obtained using various strain energy functions, the strain energy function that can best represent the material behavior of porcine liver tissue could be determined. For example, with the following Mooney–Rivlin energy function with nine material constants (known as the 9-constant theory),[43]

$$\begin{aligned} W = {} & C_1(I_1 - 3) + C_2(I_2 - 3) + C_3(I_3 - 3)^2 + C_4(I_1 - 3)(I_2 - 3) \\ & + C_5(I_2 - 3)^2 + C_6(I_1 - 3)^3 + C_7(I_1 - 3)^2(I_2 - 3) \\ & + C_8(I_1 - 3)(I_2 - 3)^2 + C_9(I_2 - 3)^3 \end{aligned}$$

where C_1, C_2, C_3, C_4, C_5, C_6, C_7, C_8 and C_9 are material constants. The stress–strain relationship could be derived by substituting W into Eq. (2). The resulting equation was highly complex, with the highest order term having a power of 6 and the lowest order term having a power of -5.

Equation (3) is the 2-constant version of the energy function for the Mooney–Rivlin material.

$$W = \frac{C_1}{2}(I_1 - 3) + \frac{C_2}{2}(I_2 - 3) \tag{3}$$

where C_1 and C_2 are material constants and C_1, $C_2 > 0$. Similarly, partial differentiation of W, with I_1 and I_2 obtained from Eq. (2) yielded the following stress–strain relation.

$$T = C_1\lambda + C_2 - \frac{C_1}{\lambda^2} - \frac{C_2}{\lambda^3}$$

whereλ is equal to strain plus one. For ease of discussion, we simply refer to $T = f(\lambda)$ as stress–strain relation. How well this stress–strain relation represented the experimental data could be evaluated using this stress–strain relation. Our assumption on isotropic, homogeneous and incompressible liver model is consistent with recent literature[13,18,35,41,42] on modeling of abdominal organs for surgical simulation.

There are several types of strain energy functions: polynomial, exponential, logarithmic and power. The Mooney–Rivlin material is an example of a strain energy function with polynomial form. The simplest polynomial-based energy function is the neo-Hookean model, which was originally applied to incompressible nonlinear elastic engineering materials. The neo-Hookean model is a subset of the Mooney–Rivlin model with $C_2 = 0$. There is only one material constant C_1 in this equation shown below:

$$W = C_1(I_1 - 3).$$

An exponential form of strain energy due to Fung[38] and Demiray[54] is shown as follows,

$$W = \frac{C_1}{2C_2}(e^{C_2(I_1-3)} - 1)$$

where C_1 and C_2 are material constants, and $C_1, C_2 > 0$.

Other exponential strain energy function includes Veronda and Westmann[44] shown as follows,

$$W = C_1(e^{C_2(I_1-3)} - 1) + C_2(I_2 - 3) + g(I_3).$$

If liver tissue is assumed as incompressible, $g(I_3) = 0$.

A related class of exponential equations with logarithmic form was proposed by Hayashi and Takamizawa.[45,46] The equation was intended for transversely anisotropic material:

$$W = -C_1 \ln\left(1 - \frac{1}{2}C_2(I_1 - 3)^2 + \frac{1}{2}C_3(I_4 - 1)^2 + C_4(I_1 - 3)(I_4 - 1)\right).$$

The corresponding logarithmic equation for isotropic material is as follows,

$$W = -C_1 \ln(1 - C_2(I_1 - 3)).$$

The main difference between isotropic version and the original Hayashi equation is the absent of invariant I_4 in the former. This invariant was not applicable with an isotropic material.

The fourth type of commonly used constitutive relation is the power law of the form $T = KS^n$ where T is the Lagrangian stress tensor, S is the strain or strain rate tensor, and K and n are the material constants. The advantage of power law stress-strain function is its simplicity. The following equation originally proposed by Tanaka and Fung[37] was used to model the zero-stress state of blood vessel walls in Xie *et al.*[47]

$$T = C_1(\lambda - 1)^{C_2}.$$

Other applications of the power law energy function include the formulation of extrafibrillar matrix of tendor material as a hyperelastic material using Odgen form of strain energy function[49] expressed by,

$$W = \sum_{n=1}^{3} \frac{C_n}{\alpha_n}(\lambda_1^{0.5\alpha_n} + \lambda_2^{0.5\alpha_n} + \lambda_3^{0.5\alpha_n}),$$

$$T = \sum_{n-1}^{3} \frac{C_n}{2}(\lambda^{\alpha_n} - \lambda^{0.5\alpha_n - 1}).$$

A variant of Odgen model was proposed in Bogen *et al.*[50] to describe passive myocardial behavior, where C_1 and C_2 are material constants. The equations were

as follows,

$$W = \frac{C_1}{C_2}(\lambda_1^{C_2} + \lambda_2^{C_2} + \lambda_3^{C_2} - 1),$$

$$\sigma = C_1(\lambda^{C_2} + \lambda^{-2C_2}).$$

The corresponding first Piola-Kirchhoff form of Bogen equation is

$$T = C_1(\lambda^{C_2 - 1} + \lambda^{-2C_2 - 1}).$$

The combined logarithmic and polynomial model[25] can be derived in the same spirit as the derivation of combined exponential and polynomial model in Fung *et al.*[51] At low strain, the logarithmic component in the combined model was small, and the polynomial component was the dominant one. Their roles were reversed at high strain. The combined logarithmic and polynomial model is therefore advantageous in describing the entire stress-strain curve. Note that the Veronda and Westmann model also has both exponential and polynomial terms. The Veronda and Westmann model was a sum of an exponential function and a polynomial originally for constitutive modeling of the skin. The combined logarithmic and polynomial equation for isotropic materials is as follows,

$$W = \frac{-C_1}{2}\ln(1 - C_2(I_1 - 3)) + C_3(I_1 - 3).$$

To simplify the discussion, we referred to this equation as the combined logarithmic and polynomial model or combined energy model.

Almost all the constitutive models provided good fits for the experimental data over the elongation region. The fits for the neo-Hookean and the Mooney–Rivlin (2-constants) were not acceptable for the purpose of fitting the entire curves. Not all equations provided good fits for the experimental compression data. The Tanaka model could not match the compression stress-strain curve since a power equation could not represent compression since the theoretical stress computed using this equation was always positive for all positive stretch ratios. Failure of these equations to match the experimental data of combined compression and elongation test was partly due the difficulties in representing both negative and positive domains numerically. A RMSE of greater than 120 Pa is considered a bad fit. The combined energy model and Mooney–Rivlin (9-constant) model were the only models that could adequately represent these data.

The best constitutive model appeared to be the combined logarithmic and polynomial equation.[25] The combined energy equation provided a good fit for the stress-strain relationships in the tests involving compression followed by elongation, as well as consistently matching the independent compression and elongation data. Although the combined model has larger RMSE than that of Mooney–Rivlin (9-constant, the former has smaller number of material constants and the parameters are numerically more stable. With Mooney–Rivlin (9-constant) model, the material parameters varied widely — a parameter could be positive in one

Table 3. Material parameters of combined energy model in representing elongation, compression and combined compression and then elongation experimental data.

$$W = \frac{C_1}{2}\ln(1 - C_2(I_1 - 3)) + C_3(I_1 - 3)$$

	Elongation	Compression	Combined Compression and Elongation
C_1	−337.7	−7881.1	−342.4
C_2	2.2	1.6	1.9
C_3	−287.7	−3941.4	−136.0

representation and negative in another. This pitfall was typical with polynomial-based constitutive equation. It could cause very different mechanical behavior in 3D cases and pose serious accuracy issues during numerical analysis such as finite element method.[48] Table 3 lists the material constants used in the combined energy model to fit the average stress–strain curve respectively from elongation, compression and combined compression and elongation experiments. More details on the curve fitting results can be found in Chui *et al.*[25]

We repeated the analyses for liver tissue with porcine kidney and brain tissues. The experimental conditions and procedures were the same for all three types of soft tissues. A close fit was possible with the combined logarithmic and polynomial model. The combined logarithmic and polynomial model could model these tissues with similar errors, and small deviations in material parameters. The polarity of the parameters did not change in the combined model. This demonstrates the suitability of our combined logarithmic and polynomial energy function as the model of choice for soft tissues in general and liver tissue in particular. The experiments with porcine kidney and brain tissues were conducted preliminary with five test samples each.

5.3. *Image based inverse finite element parameter estimation*

Although the strain energy based constitutive equations are generally valid for three-dimensional stress state, the material parameters determined in this section are limited by the uniaxial loading experiments. Typical multi-axial experiments involve frozen tissue. This will inevitably alter the biomechanics of underlying tissue. Image based inverse finite element parameter estimation could be used in conjunction with uniaxial combined compression and elongation experiments to determine the material parameters of liver tissue in three-dimensional stress state.

Figure 13(a) is a flow chart that illustrates the process. Input to the method was video images of the deformation. The video was processed and separated into individual frames of deformation with known force and time. A displacement driven axisymmetric finite element model of the tissue sample was developed to determine mechanical properties of liver tissue (Figure 13(b)). This generic model was adjusted to represent liver tissue sample height measured during experiments. The diameter

of the sample was set at 7 mm. The planar surface was assumed to be flat and bonded to the hard rubber plates. Due to asymmetry, only 1/8 of the tissue sample is required to be modelled. The model comprises of eight nodes brick elements. MARC 7 a commercially available finite element solver is used in conjunction with Patran 2001 (MSC Software Corporation, USA), a pre- and post processor for CAE simulation, in the solution process as well as material properties assignment. From the list of instantaneous parameters, a set of parameters is selected based on its ability to model the stress–strain curve.

Recall that Piola-Kirchhoff stress can be expressed in terms of energy W and Green–Lagrange strain E_{ij} as follows:

$$S_{ij} = \frac{\partial(W)}{\partial E_{ij}}.$$

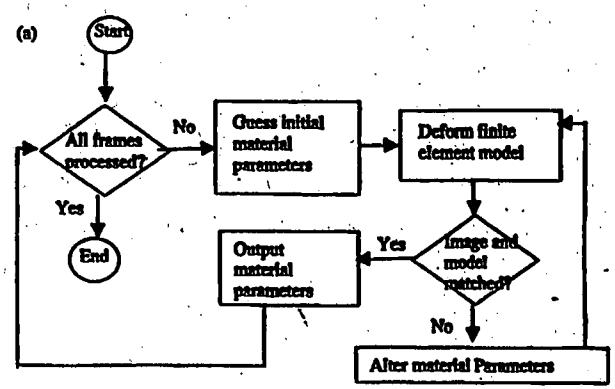

Fig. 13(a). Overview of image based inverse finite element parameters estimation: flow chart for estimation of material parameters for instantaneous deformation.

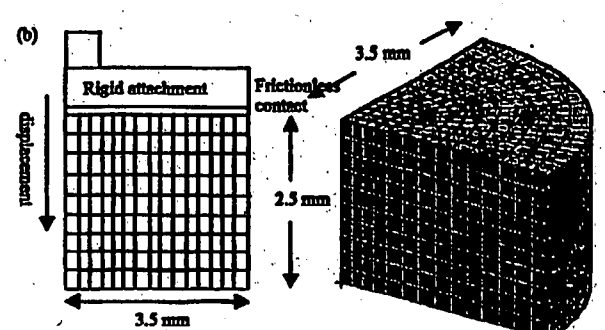

Fig. 13(b). Overview of image based inverse finite element parameters estimation: finite element modeling.

For modeling of biological soft tissue, a popular constitutive equation was the pseudo-strain-energy function proposed by Fung.[52] Following is the original generalized exponential equation where α_{ijk}, β_0, β_{mnpq}, γ_{ij} and κ_{ijkl} are constants to be determined empirically,

$$W = \frac{1}{2}\alpha_{ijk}E_{ij}E_{kl} + (\beta_0 + \beta_{mnpq}E_{mn}E_{pq})\exp(\nu_{ij}E_{ij} + \kappa_{ijk}E_{ij}E_{kl} + \cdots).$$

The derivation could be illustrated by first considering a two dimension problem space. Following equation is the simplified 2D version that is valid for the physiological range. Note that E_{12} is the shear.

$$\begin{aligned} W = {} & \frac{1}{2}(\alpha_1 E_{11}^2 + \alpha_2 E_{22}^2 + \alpha_3 E_{12}^2 + \alpha_3 E_{21}^2 + 2\alpha_4 E_{11}E_{22}) \\ & + \frac{1}{2}C\exp(\alpha_1 E_{11}^2 + \alpha_2 E_{22}^2 + \alpha_3 E_{12}^2 + \alpha_3 E_{21}^2 + 2\alpha_4 E_{11}E_{22} \\ & + \nu_1 E_{11}^3 + \nu_2 E_{22}^3 + \nu_4 E_{11}^2 E_{22} + \nu_8 E_{11}E_{11}^2). \end{aligned}$$

By having ν's terms equal to 0, the equation can be simplified further to

$$W = f(\alpha, E) + C\exp(F(\alpha, E)),$$

where

$$\begin{aligned} f(\alpha, E) &= \alpha_1 E_{11}^2 + \alpha_2 E_{22}^2 + \alpha_3 E_{12}^2 + \alpha_3 E_{21}^2 + 2\alpha_4 E_{11}E_{22}, \\ F(a, E) &= a_1 E_{11}^2 + a_2 E_{22}^2 + a_3 E_{12}^2 + a_3 E_{21}^2 + 2a_4 E_{11}E_{22}. \end{aligned}$$

If we are considering physiological range only and have no concern on very small strain, we can simplify the exponential energy function further to

$$W = C\exp(F(a, E)).$$

Assuming that liver tissue is isotropic ($E_{12} = E_{21}$),

$$F(a, E) = a_1(E_{11}^2 + E_{22}^2) + 2a_3 E_{12}^2 + 2a_4 E_{11}E_{22}.$$

Following is the corresponding exponential term in a 3D problem space. The assumption on material isotropy implies that $E_{12} = E_{21}$, $E_{23} = E_{32}$ and $E_{13} = E_{31}$. Also $a_1 = a_2 = a_3$, $a_4 = a_5 = a_6$ and $a_7 = a_8 = a_9$. This leads to

$$\begin{aligned} F(a, E) = {} & a_1 E_{11}^2 + a_2 E_{22}^2 + a_3 E_{33}^2 + a_4 E_{12}^2 + a_4 E_{21}^2 \\ & + a_5 E_{23}^2 + a_5 E_{32}^2 + a_6 E_{13}^2 + a_6 E_{31}^2 \\ & + 2a_7 E_{11}E_{22} + 2a_8 E_{22}E_{33} + 2a_9 E_{33}E_{11} \\ = {} & a_1(E_{11}^2 + E_{22}^2 + E_{33}^2) + 2a_4(E_{12}^2 + E_{23}^2 + E_{31}^2) \\ & + 2a_7(E_{11}E_{12} + E_{22}E_{23} + E_{33}E_{31}). \end{aligned}$$

Hence,

$$W = C\exp(F(a, E)),$$

where

$$\begin{aligned} F(a, E) = {} & a_1(E_{11}^2 + E_{22}^2 + E_{33}^2) + 2a_4(E_{12}^2 + E_{23}^2 + E_{31}^2) \\ & + 2a_7(E_{11}E_{12} + E_{22}E_{23} + E_{33}E_{31}) \end{aligned}$$

Note that if effect from shear is not considered then $a_4 = a_5 = a_6 = 0$. If the effect similar to Poisson's ratio is negligible, $a_7 = a_8 = a_9 = 0$.

Equivalent logarithmic energy function is given as follows:

$$W = -C\ln(F(a, E)),$$

where

$$\begin{aligned} F(a, E) = {} & \frac{a_1}{2}(E_{11}^2 + E_{22}^2 + E_{33}^2) + a_4(E_{12}^2 + E_{23}^2 + E_{31}^2) \\ & + a_7(E_{11}E_{12} + E_{22}E_{23} + E_{33}E_{31}). \end{aligned}$$

The corresponding combined logarithmic and polynomial energy function is as follows:

$$W = -\frac{C}{2}\ln(1 - F(a, E)) - \frac{C}{2}F(a, E) + \frac{F_1(a, E)}{2},$$

where

$$\begin{aligned} F(a, E) = {} & \frac{a_1}{2}(E_{11}^2 + E_{22}^2 + E_{33}^2) + a_4(E_{12}^2 + E_{23}^2 + E_{31}^2) \\ & + a_7(E_{11}E_{12} + E_{22}E_{23} + E_{33}E_{31}) \\ F_1(a, E) = {} & \frac{a_{10}}{2}(E_{11}^2 + E_{22}^2 + E_{33}^2) + a_{11}(E_{12}^2 + E_{23}^2 + E_{31}^2) \\ & + a_{12}(E_{11}E_{12} + E_{22}E_{23} + E_{33}E_{31}). \end{aligned}$$

In modeling the uniaxial tension/compression tests that we performed, the shear terms are ignored. The exponential strain energy functions in 2D problem spaces become

$$W = C\exp(F(a, E)),$$

where

$$F(a, E) = a_1(E_{11}^2 + E_{22}^2) + 2a_4 E_{11}E_{22}.$$

The corresponding equation in 3D is

$$W = C\exp(F(a, E)),$$

where

$$F(a,E) = a_1(E_{11}^2 + E_{22}^2 + E_{33}^2) + 2a_7(E_{11}E_{12} + E_{22}E_{23} + E_{33}E_{31}).$$

The equivalent logarithmic energy functions in 2D and 3D problem spaces are respectively,

$$W = -C\ln(F(a,E)),$$

where

$$F(a,E) = \frac{a_1}{2}(E_{11}^2 + E_{22}^2) + a_4E_{11}E_{22}$$

and

$$W = -C\ln(F(a,E)),$$

where

$$F(a,E) = \frac{a_1}{2}(E_{11}^2 + E_{22}^2 + E_{33}^2) + a_7(E_{11}E_{12} + E_{22}E_{23} + E_{33}E_{31}).$$

The combined logarithmic and polynomial energy function for non isotropic material in 3D space is

$$W = -\frac{C}{2}\ln(1 - F(a,E)) - \frac{C}{2}F(a,E) + \frac{F_1(a,E)}{2},$$

where

$$F(a,E) = \frac{a_1}{2}(E_{11}^2 + E_{22}^2 + E_{33}^2) + a_7(E_{11}E_{12} + E_{22}E_{23} + E_{33}E_{31}),$$

$$F_1(a,E) = \frac{a_{10}}{2}(E_{11}^2 + E_{22}^2 + E_{33}^2) + a_{12}(E_{11}E_{12} + E_{22}E_{23} + E_{33}E_{31}).$$

The inverse approach to determine liver material properties involve comparing the experimental data with theoretical stress and strain calculated using finite element method. The liver material properties are expressed in terms of material constants in various energy functions.

Figure 14(a) illustrates the comparison of images of experiments and finite element deformation of the liver tissue sample at six regular intervals. It is possible to obtain a good fit with the stress–strain curve from elongation test using appropriate material parameters as shown in Fig. 14(b).

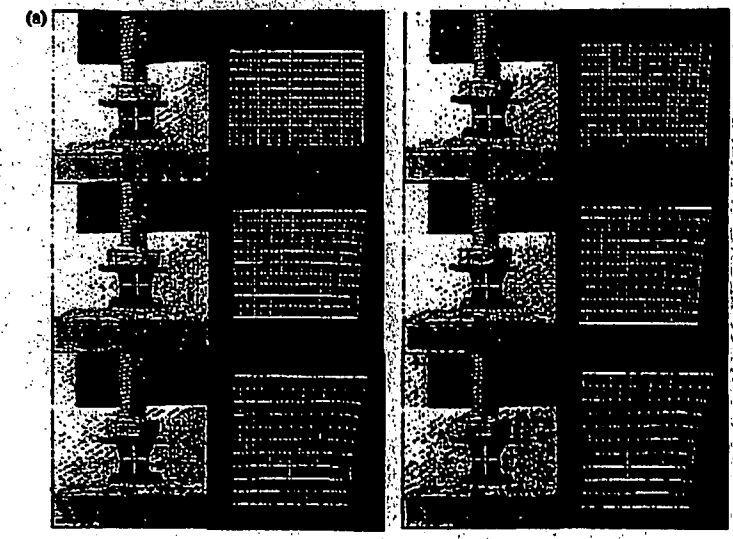

Fig. 14(a). Results from inverse finite element parameters estimation: matching of deformed model and images of experiment.

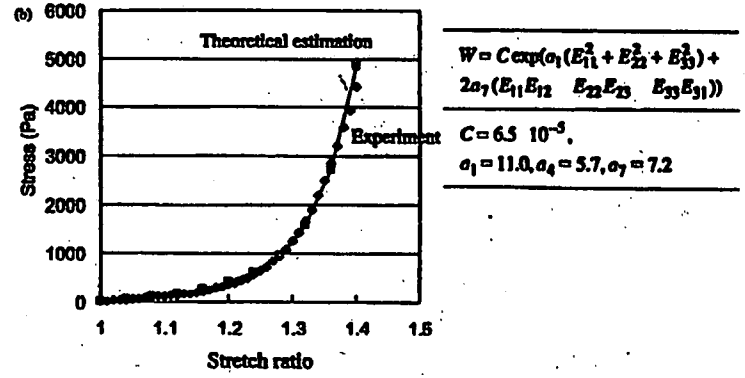

Fig. 14(b). Results from inverse finite element parameters estimation: curve fitting of experimental stress–strain curve.

5.4. *Multi-linear constitutive equation*

Fast computation with reasonable accuracy is desired in computer aided surgical simulation. A multi-linear constitutive equation defined on the concept of equivalent stress may be appropriate for such applications. The constitutive model assumes that the mechanical properties of liver tissue are isotropic and could be defined using instantiated elastic modulus and Poisson's ratio from stress–strain curve.

We refer to a cylindrical sample of liver tissue undergoing uniaxial tension and/or compression test. If the slope of σ versus ε is plotted against σ, the result was a roughly straight curve. We may fit this experimental curve by a series of straight lines, i.e.

$$\frac{d\sigma}{d\varepsilon} = \alpha_1(\sigma + \beta_1), \quad 0 \le \sigma \le \sigma_1$$
$$\frac{d\sigma}{d\varepsilon} = \alpha_2(\sigma + \beta_1), \quad \sigma_1 \le \sigma \le \sigma_2$$

An integration gives

$$\sigma + \beta_1 = c_1 \exp(\alpha_1 \varepsilon), \quad 0 \le \sigma \le \sigma_1$$
$$\sigma + \beta_2 = c_2 \exp(\alpha_2 \varepsilon), \quad \sigma_1 \le \sigma \le \sigma_2$$

and

$$\sigma = c_1 \exp(\alpha_1 \varepsilon) - \beta_1, \quad 0 \le \sigma \le \sigma_1$$
$$\sigma = c_2 \exp(\alpha_2 \varepsilon) - \beta_2, \quad \sigma_1 \le \sigma \le \sigma_2 \tag{4}$$

The integration constants can be determined by curve fitting this equation with the original experimental stress–strain curve. Stress is used to define the intervals. Strain can also be used by simply start with a curve with slope of σ versus ε is plotted against ε.

Representation of the stress–strain curve can also be done via piece-wise approximation using linear functions treating each line segment as a linear elastic material. Following is the bilinear constitutive model:

$$\sigma = E_0 \varepsilon_0, \quad \varepsilon \le \varepsilon^*$$
$$\sigma = E(\varepsilon - \varepsilon^*) + E_0 \varepsilon^*, \quad \varepsilon > \varepsilon^*,$$

where E_0 is Young's modulus at the toe region, ε^* is the strain at toe-linear region. An issue with this model is that it is very sensitive to the definition of the maximum stress. The following multi-linear constitutive model is proposed to represent the nonlinear material model.

$$\sigma = E_0 \varepsilon_0, \quad \varepsilon \le \varepsilon^*$$
$$\sigma = E_i \left(\varepsilon_i - \sum_{j=0}^{i-1} \varepsilon_j \right) + \sum_{j=0}^{i-1} E_j \varepsilon_j, \quad \varepsilon > \varepsilon_i^*,$$

To define the intervals ε_i, curve fitting was applied on the $d\varepsilon - \sigma$ curve with Eq. (4). A region/interval was established when the residual error from the fitting

was greater than a tolerance. In this study, a very small tolerance of 0.00001 was used.

$$\sigma = C_1(\varepsilon + C_2) = C_1\varepsilon + C_3$$

where C_1, C_2 and $C_3 = C_1C_2$ are constants, and $d\varepsilon$ is the Young's modulus. Hence, the relation at each interval is expressed in terms of straight lines. The parameter C_1 represents the rate of increase of the elastic modulus with respect to increasing tension or compression corresponding to the slope of the curve. The parameter C_3 is the intercept of the straight-line segment extended to zero stress.

Note that unloading at the same strain rate results in similar straight lines with different slopes. In view of the significant difference during loading and unloading of liver tissue, loading and unloading should be in fact considered as two different materials. Only loading curve is considered. The multi-linear constitutive model is a more direct approach compared to the exponential based method and is the focus of this section. Multi-linear constitutive model is also applicable to Poisson's ratio. However, the Poisson's ratio of liver tissue was found to vary around 0.5, and considering the infusion of blood in patient's liver organ, we assume that liver tissue is incompressible.

5.4.1. *Equivalent stress and strain for multi-axial state*

The constitutive equations described above are often good practical choices for fast surgical simulation with less emphasis on accuracy. They do not reduce to the form of strain energy and generally are not valid for three dimensional stress states. To relate the uniaxial stress–strain relationship represented by these constitutive equations with the general multi-axial stress–strain relationship, equivalent stress and strain is proposed as the "bridge" for this correlation.

The engineering stress T is the load F divided by the cross-sectional area of the specimen at zero stress state, A_0. The engineering strain e is defined as the ratio between displacement $(L_f - L_0)$ and the original length of the specimen L_0. T and e were measured in our experiments. As was described earlier, liver tissue being a nonlinear material, true or nature stress σ and strain ε should be used since we seek to model large strain deformation. The following definitions for true stress and strain are used.

$$\varepsilon = \int_0^{\varepsilon} dE = \int_{L_0}^{L_f} \frac{dL}{L} = \ln \frac{L_d}{L_0} \tag{5}$$

where dL is the incremental change and L is the length at beginning of increment.

$$\sigma = \frac{F}{A}$$

where A is the instantaneous cross sectional area of the deformed specimen. From Eq. (5) and definition of engineering strain, we arrived at the following relationship between engineering and true strain,

$$\varepsilon = \ln(1+e). \tag{6}$$

Similarly, the following relationship between engineering and true stress can be established,

$$\sigma = T(1+e).$$

After determining the true stress and stress from uniaxial experiment, it is necessary to relate this uniaxial observation to stress and strain in the general state. For this purpose, we assume that for any given stress state, there exists an equivalent uniaxial stress state generally associated with plastic deformation.[51] For realistic simulation of 3D deformation, it is suffice to define six stress components $(\sigma_x, \sigma_y, \sigma_z, \tau_{xy}, \tau_{yz}, \tau_{zx})$ and six strain components $(\varepsilon_x, \varepsilon_y, \varepsilon_z, \nu_{xy}, \nu_{yz}, \nu_{zx})$ under multi-axial stress-strain state. The equivalent stress σ_e, also known as von Mises stress and equivalent strain ε_e are defined as follows

$$\sigma_e = \frac{1}{\sqrt{2}}((\sigma_x-\sigma_y)^2+(\sigma_y-\sigma_z)^2+(\sigma_z-\sigma_x)^2+6(\tau_{xy}^2+\tau_{yz}^2+\tau_{zx}^2)).$$

$$\varepsilon = \int d\varepsilon_e,$$

where $d\varepsilon_e$ is the strain increment defined as follows

$$d\varepsilon_e = \frac{\sqrt{2}}{3}((d\varepsilon_x-d\varepsilon_y)^2+(d\varepsilon_y-d\varepsilon_z)^2+(d\varepsilon_z-d\varepsilon_x)^2+6(d\nu_{xy}^2+d\nu_{yz}^2+d\nu_{zx}^2)).$$

During finite element simulation with multi-axial state of stress, the computed stress of the finite element will be first converted to the equivalent stress. This is to select the appropriate region in the multi-linear constitutive model for representation of the material properties of the soft tissue at the finite element. Under uniaxial state of stress,

$$\sigma_x = \sigma$$
$$\sigma_x = \sigma_y = \tau_{xy} = \tau_{yz} = \tau_{zx} = 0.$$

We assume that liver is isotropic and incompressible. Hence,

$$\varepsilon_x = \varepsilon$$
$$\varepsilon_x = \varepsilon_y = -\frac{\varepsilon}{2}$$
$$\nu_{xy} = \nu_{yz} = \nu_{zx} = 0.$$

Since $\sigma_e = \sigma_x = \sigma$ and similarly for strain, followed by integration by parts,

$$\varepsilon_e = \int d\varepsilon = \varepsilon.$$

Hence, it is suffice for us to assume that the equivalent stress is the true stress and equivalent strain is the true strain under uniaxial state of stress and strain.

Figure 15 illustrated the variation of elastic modulus calculated from average true stress and strain curves with true stress during compression and elongation test. The variation in elongation was relatively smaller and could be represented using several straight lines. Nevertheless, in the case of compression, we observed much disparity in the fitting the experiment data with straight lines. More straight lines were required to fit this experimental data. The variations defined the intervals where elastic modulus is desired.

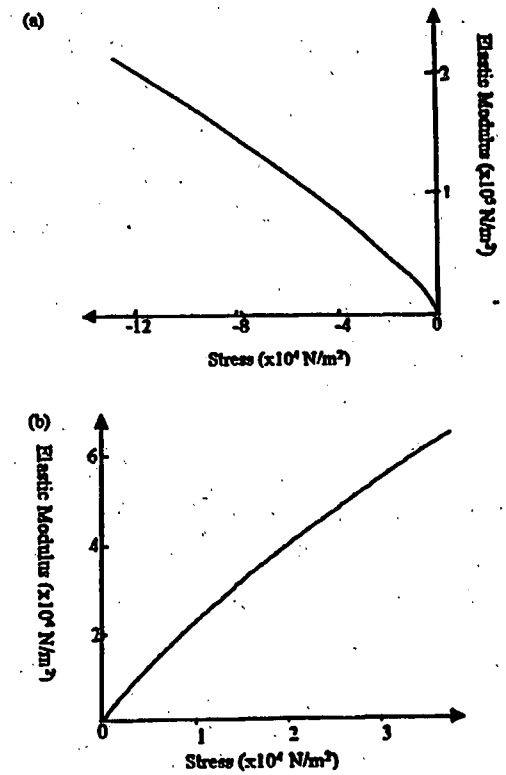

Fig. 15. Variation of elastic modulus with stress for (a) elongation and (b) compression. The stress for elongation and compression was an average of the data listed in Table 1 and Table 2 respectively.

Table 4. Material parameters of equivalent stress and strain based multi-linear constitutive model.

$$\sigma = E_0 \varepsilon_0, \quad \varepsilon \le \varepsilon_0$$
$$\sigma = E_i \left(\varepsilon_i - \sum_{j=0}^{i-1} \varepsilon_j \right) + \sum_{j=0}^{i-1} E_j \varepsilon_j, \quad \varepsilon > \varepsilon_i$$

Strain Intervals, ε_i	Elastic Modulus, E_i($\times 10^4$ N/m^2)	Stress Intervals ($\times 10^4$ N/m^2)
−0.57 to −0.60	−424.133	−11.067 to −12.724
−0.55 to −0.57	−553.350	−9.180 to −11.067
−0.52 to −0.55	−305.999	−6.348 to −9.180
−0.48 to −0.52	−158.699	−4.887 to −6.348
−0.46 to −0.48	−244.380	−3.404 to −4.887
−0.42 to −0.46	−85.112	−2.101 to −3.404
−0.36 to −0.42	−35.018	−0.887 to −2.101
0.00 to −0.36	−2.465	0.00 to −0.887
0.00 to 0.38	1.176	0.00 to 0.447
0.38 to 0.43	17.600	0.447 to 0.880
0.43 to 0.48	34.740	0.880 to 1.737
0.48 to 0.52	63.699	1.737 to 2.548
0.52 to 0.54	148.154	2.548 to 2.963
0.54 to 0.58	95.502	2.963 to 3.820

6. Finite Element Simulation of Soft Tissue Deformation

Accuracy and computational time are two main constraints in the practical application of soft tissue modeling. Depending on the applications, there are different requirements in these two criteria. Typically, simulation for surgical planning may have from 30 s to 1 h to deliver a clinically relevant result for outcome prediction. A surgical procedure training system will have computational time in the order of 0.1 s to achieve smooth user interaction whereas accuracy of deformation is not necessary of primary important. There were interactive computer simulations based on techniques in biomechanical engineering and computer graphics, e.g.[55]

An approach in simulation of soft tissue deformation is via finite element method. Finite element based simulation of soft tissue deformation have been applied both in surgical simulators[6,56,57] as well as elastic image registration.[58,59] The multi-linear constitutive equation is an appropriate material model for surgical training application that demands fast computation with reasonable accuracy. The strain energy based constitutive equations should be used when higher accuracy is desired.

The main motivation of employing von Mises stress in multi-linear constitutive model is its ability to predict nonlinear stress–strain relationship at and after yield point. In order to validate the hypothesis of our scheme in relating the multi-axial stress and strain with that measured during uniaxial experiments, independent experiments were conducted, and the recorded experimental deformation were

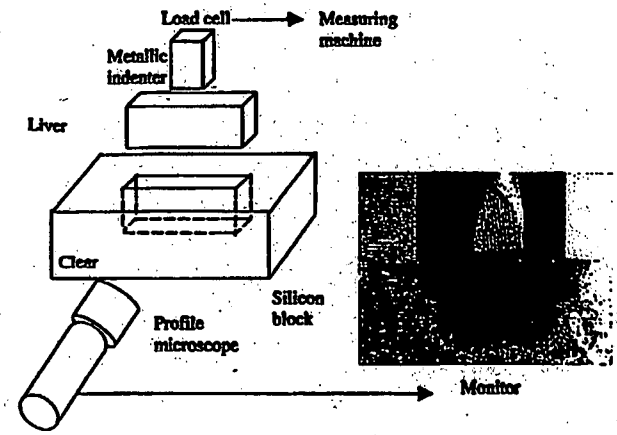

Fig. 16. *In vitro* experiment with multi-axial deformation. Tissue of rectangular shape was extracted from porcine liver organ and placed inside a hole of the same size in a silicon block. The deformation of the liver tissue was recorded using a profile microscope. Insert is snap shot of experimental tissue sample at zero stress state.

compared with that of the corresponding finite element simulation using the multi-linear constitutive equation described above. The experimental setup (Fig. 16) was similar to that of our uniaxial experiment described earlier. A rectangular block of porcine liver tissue sample with dimension 30 mm × 10 mm × 10 mm was used in an indentation test. The test resembles the multi-axial structure problem involving local load on half space. A uniform load from an indenter with a square base (10 mm × 10mm) was applied on the top surface of the sample. The sample was placed in a transparent silicon block with dimension 30 mm × 10 mm × 10 mm. Recording of the deformation was done using a profile microscope. The loading rate and other conditions were the same as that of the compression and elongation tests at 10 mm/min.

Figure 17 shows finite element simulation of the rectangular block sample, and corresponding deformation on the X–Y plane recorded at various time steps. In this simulation, we use MARC 7 for finite element analysis and Patran 2001 as pre- and post processor. There were a total of 657 TETRA4 elements and 208 nodes in the model. The material was represented using the multi-linear constitutive model. Boundary conditions are imposed at the bottom and the four sides. Since the deformation is relatively large at 1 mm, 2 mm and 3 mm, geometrical nonlinear condition was imposed and hence, a nonlinear solver was used in the solution process. The simulated deformations were compared with the recorded images during the experiment. It was observed that the deformation from finite element simulation consistently smaller than that of the recorded images by an almost

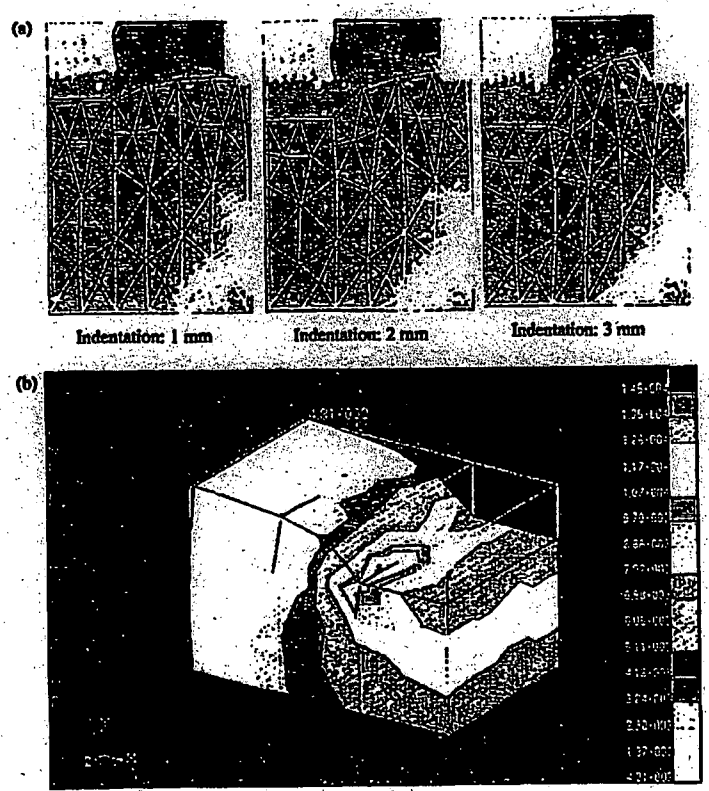

Fig. 17. Finite element simulation of multi-axial deformation experiment. (a) The simulated deformation (drawn with mesh lines) is compared with the recorded deformation at various instants. (b) Equivalent stress distribution at 3 mm indentation.

constant area. This inconsistency was possibly due to the imperfect condition of the experiments. For example, friction was not considered in the computational study. Although precaution have been taken to avoid the liver tissue becoming dry, friction was inevitable. Nevertheless, this shortfall is rather consistent. The simulation is reasonably accurate if this offset is considered.

To quantitatively evaluate the "match" between the computational and experimental deformation, we use the root-mean-square value of the residual as the quantitative standard error indicator for the match. Residual can be defined as the difference between the observed and predicted data. Suppose that A is the residual of deformed contors predicted by the computational method and experimental method. The root-mean-square value is equal to $\text{norm}(A)/\sqrt{n}$ where n is the number of

elements in A, and $\text{norm}(A) = \sqrt{\sum A^2}$. The standard error for the deformation at deformation 1 mm, 2 mm and 3 mm are: in x direction — 0.48 mm, 1.15 mm and 2.02 mm; in y direction — 0.63 mm, 1.11 mm and 0.22 mm. The average percentage of error is 8% and 4 % respectively. The relatively small error prompted us to believe that the computational deformation will match the corresponding experimental deformation if the rather consistent shortfall described in previous paragraph has been taken care off. Hence, the validity of using equivalent stress and strain as the "bridge" to transform the uniaxial experiment and constitutive model to the general multi-axial state was demonstrated.

The strain is generally greater than 10% during surgical simulation. This is large deformation by definition. Numerically, static finite element method, also known as small strain theory, does not apply here. In this case, finite element method based on finite deformation should be used. In the previous paragraph, the nonlinear solver takes an average CPU time of 0.1 s for a 17 steps deformation analysis on an Intel Pentium III 1.2 GHz notebook computer. This is equivalent to about 10 frames per second. Figure 18(a) is a high resolution finite element model of human liver organ. Figure 18(b) shows the corresponding low resolution finite element model deformed under force applied from the front with a large probe. The deformation is near real time with approximately 12 frames per second using a customized nonlinear finite element code. It might be possible to achieve real time interaction for the high resolution model if deformation can be considered local and small strain theory is applicable.

The requirement of fast computation prompted many investigators to exploit the possible use of small strain theory in medical simulation. For application of small strain theory, we can divide the large deformation into a number of much smaller displacement steps. For each small displacement step, the strain components are computed using Cauchy's infinitesimal strain tensor formula. Note that in this case, the incremental errors introduced by small strain formulation were assumed to be

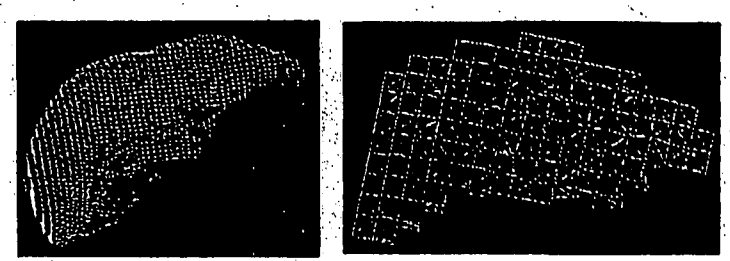

Fig. 18. Finite element modeling and simulation of human liver organ. (a) High resolution finite element model; (b) deformation of low resolution finite element model of liver with 3470 linear tetrahedral elements and 1079 nodes.

small and can be neglected

$$\epsilon_x = \frac{\partial u}{\partial x}, \quad \epsilon_y = \frac{\partial v}{\partial y}, \quad \epsilon_z = \frac{\partial w}{\partial z}$$

$$\nu_{xy} = \frac{1}{2}\left(\frac{\partial u}{\partial y} + \frac{\partial v}{\partial x}\right), \quad \nu_{yz} = \frac{1}{2}\left(\frac{\partial v}{\partial z} + \frac{\partial w}{\partial y}\right), \quad \nu_{xz} = \frac{1}{2}\left(\frac{\partial u}{\partial z} + \frac{\partial w}{\partial x}\right),$$

where $u = u(x, y, z)$, $v = v(x, y, z)$ and $w = w(x, y, z)$ are the displacement fields in the x, y and z directions respectively, from one small displacement iteration to another. Nodal stress in the finite element is then computed using conventional linear finite element method.

Figure 19 illustrates a 2D deformation of the liver due to needle insertion using the small strain theory and the multi-linear constitute model. A frictionless contact was assumed. We also assume that a node fails when the stress at the node is greater

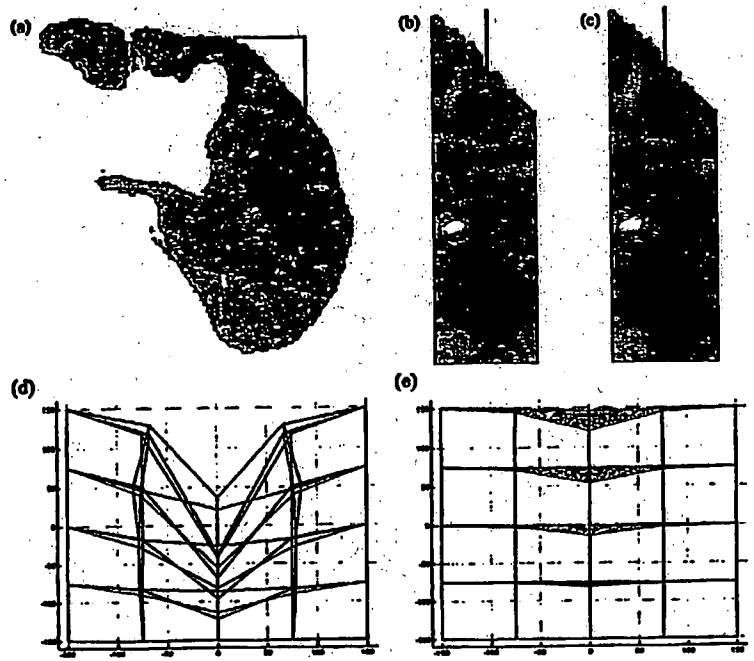

Fig. 19. Finite element simulation of liver deformation due to needle insertion: (a) planar view of a human liver with a synthesized tumor; (b) deformation of liver surface due to insertion of needle; (c) deformation and subsequent cutting of liver tissue during needle insertion; (d) view of the deformation sequence using multi-linear model; (e) view of the deformation sequence using linear elastic model.

than the break stress of liver during compression (2.313×10^5 Pa). In Fig. 19(b), the liver surface was first deformed by the introduction of a needle. The deformation of the liver continues until the maximum stress of the liver tissue reached in Fig. 19(c). Figures 19(d) and 19(e) compares the deformation sequence from the multi-linear model and that of the linear elastic model a constant Young's modulus at 625 kPa (see Sec. 4). The former agrees with the nonlinear force–displacement behavior of liver tissue during deformation and is clearly closer to the deformation observed during surgery.

7. Concluding Remarks

An experimental approach can be adopted in the study of biomechanical modeling for computer aided surgical simulation. The approach involves deriving the theoretical models based on experimental results from customary designed experiments, and validating surgical simulation that are based on these models using experiments. The focus of this study is on liver organ.

Understanding the biomechanics of liver is important in virtual reality based surgical simulation as well as actual surgical intervention and medical image registration.[59–61] Various methods on measuring and modeling of tissue for computer aided surgery have been reported in the literature. These include simple poking interaction using biological or phantom tissue, e.g.[62,63] viscoelastic characterization of tissue, e.g.[64] as well as uniaxial loading and indentation experiments with porcine liver.[19,20,25,26] To validate the biomechanical model, Howe and colleagues developed a phantom known as "Truth Cube".[65] However, the truth cube does not consider tissue probing and cutting which are among the most common surgical tasks. Recent study[66] has attempted to compare human and porcine kidney tissues. It is generally believe that the mechanical properties of human and porcine liver tissues are similar.

Validation of computer aided surgical application is itself a challenging problem. In order to have adequate validation of, e.g. needle insertion, we need to track the needle path possibly using some imaging modalities, among the many practical issues to be considered. Although we are confident of the clinical viability of the biomechanical model and simulation, there remain some challenging research issues that warrant further investigation.

7.1. *Methods of experiment*

There are limitations with the uniaxial elongation or compression experiments in this study. The alternative multi-axial tests will subject the tissue sample to tremor such as extensive cutting and possibly freezing. We have conducted independent experiments and found that freezing will cause significant changes to the mechanical properties of liver tissue. Hence, we are of the view that uniaxial test is a feasible and preferred

approach in this context. Given that the standard deviation of the experimental stress–strain data was high, it is important to improve the accuracy of subsequent numeric computations in analysis. A possible statistical method is normalization which is a process of scaling the numbers in a data set. A way to normalize the stress–strain data is to center the strain data at zero mean and scale it to unit standard deviation. The "goodness" of fit could be improved with the normalized stress–strain curve. The standard errors in curve fitting should be smaller.

To relate the general multi-axial state in 3D deformation with the stress–strain relation from uniaxial test, the concept of equivalent stress and strain could be used as the intermediate layer. The mechanical properties of liver tissue can possibly be defined upon the lower level liver lobules. The work on measuring and modeling the mechanical properties of liver lobules is on going. Relating tissue at macro and micro scales were previously investigated by Vawter *et al.*[67] for lung.

An interesting topic for our future pursuit in experimental biomechanics is to measure the mechanical properties of liver cells and investigate their relationship with the liver lobule and the liver tissue. Preparation of the liver cell sample and the associated engineering issues such as micromanipulator control are problems that we have faced in our attempted investigation beyond liver lobule.

7.2. *Viscoelastic properties of liver tissue and constitutive modeling*

The fact that there is considerable difference in stress response to loading and unloading implies that the history of strain affects the stress, and hence, liver tissue is a viscoelastic material. As first approximation, the viscoelastic properties are assumed to be negligible. This assumption is supported by the observation that the liver tissue is relatively strain rate independent. The contribution of linear viscoelasticity is small relative to overall mechanical properties, particularly for computer aided surgical simulation when the strain rate has less variation and is only moderate quantitatively. Nevertheless, by incorporating the viscoelastic properties of liver tissue into the study will inevitably improve the proposed model.

From our experiments, the average relaxation times for constant strain and stress after compression and elongation are 6.9 s, 51.2 s and 17.5 s, 24.0 s respectively. The corresponding relaxation modulus for compression and elongation are 45.9 N/m and 101.1 N/m respectively with a standard linear solid (or Kelvin model). The resultant stress–strain relationship can barely represent up to 10% of the strain. The study reveals that a linear viscoelastic model is possibly not adequate. Liver is a highly nonlinear viscoelastic material. A nonlinear viscoelastic model which is very computational intensive is required for high accuracy.

The viscoelastic properties and shear forces of soft biological tissue were considered in some recent studies on constitutive equations for liver tissues, e.g. Refs. 68 and 69. There were more studies on viscoelastic properties of brain tissues, e.g. Refs. 70 and 71 since brain tissue is more viscous. Viscoelastic behaviors of liver

tissue sample had also been detected in our relaxation and creeping tests, and were reported in Ref. 26. We are in the process of introducing a strain rate dependent component into the combined energy constitutive model. This effort to include the nonlinear viscoelastic effect of liver tissue will be done keeping the computation cost as low as possible so that the model remains feasible for computer aided surgical simulation.

7.3. *Hepatic blood flow and biphasic poroelastic constitutive modeling*

Load testing with an extremely vascular organ such as liver (0.4–1 L of blood, 80% of mass is from cells) under *ex vivo* conditions could produce elastic and viscous behaviors that are different from *in vivo* conditions.[72,73] Liver is very unique in its microanatomy relative to hepatic arterial, portal venous (unique dual input supply) and hepatic venous blood with interconnecting lobular sinusoidal anatomy. Other organs will behave differently when distended with blood under normal vascular pressures.

A living liver is porous, and possibly a biphasic poroelastic model may better represent the experimental data if liver tissues are submerged in circulating Ringer's solution during experiment. To our best knowledge, poroelastic model has not been applied to represent liver's mechanical properties. In addition to its complexity, the poroelastic model has its limitation in biological application — unlike engineering materials such as porous rock, the fluid flow through tiny vessels in the case of liver tissue. These micro-vessels known as capillaries have tangible walls that have different mechanical properties compared to that of liver tissue comprising mainly liver cells. Furthermore, the vascular system is a closed system. Blood perfusing tissue produces an internal pressure or tension that is different from that produced by just perfusing the tissue and letting the perfusate exit through exposed and open vessels as will always be the case when biopsy like samples are tested. In order to approach what occurs in the living body, experiments on a whole intact liver will have to be conducted. Nevertheless, the boundary conditions will be extensive and meaningful data analysis may not be possible.

7.4. *Biomechanics of hepatic vessel*

An alternative will be to separately consider the biomechanics of liver tissue and the vessels in which the blood flow. Modeling of the extensive micro-vessels that flow out from the primary hepatic vascular network is the next step for vascular network modeling. To handle the small sizes and highly irregular shapes of these vessels, statistically geometrical modeling technique is possibly a good approach compared to conventional techniques.

In Conclusion, much work has been accomplished and yet much work remains to be done. Computer aided surgery is a young field — this term originated in the

early 1980s. In recent years, scientists and engineers have paid much attention to applying the physical principles and engineering methods to the behavior of parts of human body, considering it as both a structure and a machine, particularly in computer aided surgical simulation. However, it soon become apparent that what have be taken for granted in conventional engineering no longer necessarily applies.

The passive material properties of biological tissues are not linearly elastic. As is shown here, the liver tissue is non-homogeneous, possibly incompressible, highly nonlinear, largely nonlinear viscoelastic and transversely isotropic. The liver tissue is rather porous and the interstitium is filled with fluid. When all of these factors are coupled, the problem of how to describe the mechanical properties of liver tissue in a simple and accurate mathematical form for computer aided surgery becomes quite acute. Furthermore, as a living organism, liver tissue responses to stress and strain biologically as well as mechanically. The complexity of modeling will increase when considering diseased organs where the technology will find most useful application. Surgeons do not operate on normal organs so future work needs to consider how conditions such as cirrhosis/fibrosis, inflammation, infection or lesions such as tumors or cysts need to be eventually incorporated into the biomechanical modeling process. This is a difficult task and will require diseased human fresh autopsy or experimental animal tissue samples. It is only natural to start on normal tissue, but eventually, disease processes need to be considered, especially when considering the interactions of instruments and the tissue.

Knowledge of anatomy and physiology is as important as the engineering principles in biomechanics. The various constitutive equations described here, with hypothesis ranging from linear elastic, hyperelastic, multi-linear, viscoelastic to porous materials, represent only a modest effort in this challenging field. The various sophisticated approaches in biomechanics for engineering analysis may not be done at interactive speeds demanded by typical computer aided surgical application, but it is often desirable to interact with the simulation as it happens to steer the computation so as to improve treatment outcomes. Advancement in computational techniques coupled with the advancement in computing hardware may remedy the often conflicting requirement of accuracy and interactivity. This will contribute to the further integration of biomechanics with computer simulation in computer aided surgery.

Acknowledgments

This work is partially supported by "Research for the Future Program (JSPS-RFTF 99I00904)" funded by Japan Society for the Promotion of Science and "Research on medical devices for analyzing, supporting and substituting the function of human body" funded by Ministry of Health, Labor and Welfare. We would like to acknowledge the following individuals in University of Tokyo for their contributions to this ongoing scientific endeavor: Dr. Etsuko Kobayashi, A/Prof. Xien Chen, Prof. Toshiaki Hisada, Mr. Yosuke Nishimura and Mr. Kengo Mayumi. Valuable comments on the drafts from Prof. James H. Anderson, Johns Hopkins University School of Medicine, Dr. Chee-Cheon Chui, Defence Science Organization, Singapore and Prof. Teoh Swee Hin, National University of Singapore, Singapore were appreciated.

References

1. R. B. Metson, M. J. Cosenza and M. J. Cunningham, Physician experience with an optical image guidance system for sinus surgery, *Laryngoscope* 110(6) (1995) 972–976.
2. G. Burdea, *Force and Touch Feedback for Virtual Reality* (Wiley, New York, 1996).
3. P. N. Brett, C. A. Fraser, M. Henningan, M. V. Griffiths and Y. Kamel, Automated surgical tools for penetrating flexible tissue, *IEEE Eng. Med. Biol.* (1997) 264–270.
4. J. M. Rolfe and K. J. Staples, *Flight Simulators* (Cambridge University Press, England, 1986), pp. 232–249.
5. J. Wachtel, The future of nuclear plant simulation in the United States, in *Simulation for Nuclear Reactor Technology*, D. G. Walton, ed. (Cambridge University Press, England, 1985), p. 339–349.
6. J. H. Anderson, C. Chui, Y. Cai, Y. Wang, Z. Li, X. Ma, W. L. Nowinski, M. Solaiyappan, K. Murphy, P. Gailloud and A. Venbrux, Virtual reality training in interventional radiology — the Johns Hopkins and Kent Ridge Digital Laboratory experience, *Semin. Interven. Radiol.* 19(2) (2002), 179–185.
7. C. Chui, J. H. Anderson and W. L. Nowinski, A simulation system to design and evaluate patient-specific interventional radiology medical devices, in *Business Briefing: Medical Device Manufacturing and Technology* (World Markets Research Centre, United Kingdom, 2002).
8. Y. Cai, C. Chui, X. Ye, J. H. Anderson, K. M. Liew and I. Sakuma, Simulation-based virtual prototyping of customized catheterization devices, *ASME J. Comput. Inform. Sci. Eng.* 4 (2004) 132–139.
9. K. Miller and K. Chinzei, Modeling of soft tissues deformation, *J. Comput. Aided Surg.* 1(Suppl.) (1995) 62–63.
10. I. Sakuma, T. Awao, K. Masamune, T. Nakagori, T. Asano, H. Inada and T. Dohi, Passive navigation system for precise positioning of a needle electrode in radio frequency ablation, *Proc. Comput. Assisted Radiol. Surg.* (2000), p. 978.
11. D. Sorid and S. K. Moore, The virtual surgeon, *IEEE Spectrum* (2000), pp. 26–31.
12. D. L. G. Hill, C. R. Maurer, R. J. Maciunas, J. A. Barwise, J. M. Fitzpatrick and M. Y. Wang, Measurement of intraoperative brain surface deformation under a craniotomy, *Neurosurgery* 43(2) (1998) 514–526.
13. F. J. Carter, T. G. Frank, P. J. Davies, D. McLean and A. Cuschieri, Biomechanical testing of intra-abdominal soft tissue, *Med. Image Anal.* 5 (2001) 231–236.
14. R. Muthupillai, D. J. Lomas, P. J. Rossman, J. F. Greenleaf, A. Manduca and R. L. Ehman, Magnetic resonance elastography by direct visualization of propagating acoustic strain waves, *Science* 269(99) (1995) 1854–1857.
15. A. P. Pathak, M. B. Silver-Thorn, C. A. Thierfelder and T. E. Prieto, A rate-controlled indentor for *in vivo* analysis of residual limb tissues, *IEEE Trans. Rehabilitation Eng.* 6(1) (1998) 12–20.
16. S. K. Kyriacou, C. Schwab and J. D. Humphrey, Finite element analysis of nonlinear orthotropic hyperelastic membranes, *Comput. Mech.* 18 (1996) 269–278.

17. M. Kauer, V. Vuskovic, J. Dual, G. Szekely and M. Bajka, Inverse finite element characterization of soft tissue, *Proc. MICCAI 2001, LNCS 2208* (Springer–Verlag, New York, 2001), pp. 128–136.
18. P. J. Davies, F. J. Carter and A. Cuschieri, Mathematical modelling for keyhole surgery simulation: A biomechanical model for spleen tissue, *IMA J. Appl. Math.* 67 (2002) 41–67.
19. H. Tie and J. P. Desai, A biomechanical model of the liver for reality-based haptic feedback, *MICCAI(1) 2003, LNCS 2878* (Springer–Verlag, New York, 2003), pp. 75–82.
20. K. Onodera, X. Chen, T. Hisada, Identification of biomechanical material properties of soft tissues, *Proc. Jpn. Comput. Eng. Soc. Ann. Conf.* 2001 (Tokyo, Japan, 2001), (in Japanese).
21. J. Kim and M. A. Srinivasan, Characterization of viscoelastic soft tissue properties from *In vivo* animal experiments and inverse FE parameter estimation, in *Proceedings MICCAI 2005, LNCS 3750*, J. Duncan and G. Gerig, eds. (Springer–Verlag, New York, 2005), pp. 599–606.
22. Y. Fung, *Biomechanics — Mechanical Properties of Living Tissues*, Second Edition (Springer–Verlag, New York, 1993).
23. H. Yamada, *Strength of Biological Materials* (Williams & Wilkins, Baltimore, USA, 1970).
24. K. Miller and K. Chinzei, Constitutive modelling of brain tissue: Experiment and theory, *J. Biomech.* 30(11/12) (1997) 1115–1121.
25. C. Chui, E. Kobayashi, X. Chen, T. Hisada and I. Sakuma, Combined compression and elongation experiments and nonlinear constitutive modeling of liver tissue for surgical simulation, *IFMBE J. Med. Biolog. Eng. Comput.* 42(6) (2004) 787–798.
26. I. Sakuma, Y. Nishimura, C. Chui, E. Kobayashi, H. Inada, X. Chen and T. Hisada, *In vitro* measurement of mechanical properties of liver tissue under compression and elongation using a new test piece holding method with surgical glue, in *Surgical Simulation and Soft Tissue Modeling, LNCS 2673*, N. Ayache and H. Delingette, eds. (Springer–Verlag, New York, 2003), pp. 284–292.
27. K. Hayashi, N. Stergiopulos, J.-J. Meister, S. E. Greenwald and A. Rachev, Techniques in the determination of the mechanical properties and constitutive laws of arterial walls, in *Cardiovascular Techniques*, C. Leondes, ed. (CRC Press, 2001), Chapter 6.
28. C. Bruyns and M. Ottensmeyer, Measuring soft-tissue mechanical properties to support development of a physically based virtual animal model, in *MICCAI 2002, LNCS 2488*, T. Dohi and R. Kikinis, eds. (Springer–Verlag, New York, 2002), pp. 283–289.
29. G. J. Tortora, *Principles of Human Anatomy*, 9th Edition (John Wiley & Sons, 2002).
30. D. Haemmerich, I. dos Santos, D. J. Schutt, J. G. Webster and D. M. Mahvi, *In vitro* measurements of temperature-dependent specific heat of liver tissue, *Med. Eng. Phys.* 28(2) (2006) 194–197.
31. K. J. Chua, S. K. Chou and J. C. Ho, An analytical study on the thermal effects of cryosurgery on selective cell destruction, *J. Biomech.* 40(1) (2006) 100–116.
32. C. Chui, Y. Nishimura, E. Kobayashi, H. Inada and I. Sakuma, A medical simulation system with unified multilevel biomechanical model, *Proc. 5th Asian Pacific Cong. Med. Biolog. Eng.* 2002 (CDROM).
33. J. Vossoughi, Constitutive modelling of biological materials, in *The Biomedical Engineering Handbook*, J. D. Bronzino, ed. (CRC Press, 1995), pp. 263–272.

34. P. J. Davies, F. J. Carter, D. G. Roxburgh and A. Cuschieri, Mathematical modelling for keyhole surgery simulations: Spleen capsule as an elastic membrane, *J. Theoret. Med.* 1 (1999) 247–262.
35. K. Miller, Constitutive modelling of abdominal organs, *J. Biomech.* 33 (2000) 367–373.
36. J. W. Melvin, R. L. Stalnaker and V. L. Roberts, Impact injury mechanisms in abdominal organs, *SAE Trans.* 730968 (1973) 115–126.
37. T. T. Tanaka and Y. C. Fung, Elastic and inelastic properties of the canine aorta and their variation along the aortic tree, *J. Biomech.* 7(4) (1974) 357–370.
38. Y. Fung, Elasticity of soft tissues in simple elongation, *Am. J. Physiol.* 213 (1967) 1532–1544.
39. R. M. Kenedi, T. Gibson and C. H. Daly, Bioengineering studies of human skin: the effects of unidirectional tension, in *Structure and Function of Connective and Skeletal Tissue*, S. F. Jackson, S. M. Harkness and G. R. Tristram, eds. (Scientific Committee, St. Andrews, Scotland, 1964), pp. 388–395.
40. M. D. Ridge and V. Wright, The description of skin stiffness, *Biorheology* 2 (1964) 67–74.
41. F. R. Schmidlin, M. Thomason, D. Oller, W. Meredith, J. Moylan, T. Clancy, P. Cunningham and C. Baker, Force transmission and stress distribution in a computer simulated model of the kidney: An analysis of the injury mechanisms in renal trauma, *J. Trauma* 40 (1996) 791–796.
42. M. Farshad, M. Barbezat, F. Schmidlin, L. Bidaut, P. Niederer and P. Graber, Material characterization and mathematical modeling of the pig kidney in relation with biomechanical analysis of renal trauma, *Proc. North Am. Cong. Biomech.* (Waterloo, Ontario, Canada, 1998).
43. M. Mooney, A theory of large elastic deformation, *J. Appl. Phys.* 11 (1940) 582–592.
44. D. R. Veronda and R. A. Westmann, Mechanical characterizations of skin-finite deformations, *J. Biomech.* 3(1) (1970) 111–124.
45. K. Takamizawa and K. Hayashi, Strain energy density function and uniform strain hypothesis for arterial mechanics, *J. Biomech.* 20(1) (1987) 7–17.
46. K. Hayashi, Experimental approaches on measuring the mechanical properties and constitutive laws of arterial walls, *ASME J. Biomech. Eng.* 115 (1993) 481–487.
47. J. Xie, J. Zhou and Y. Fung, Bending of blood vessel wall: Stress-strain laws of the intima-media and adventitial layers, *ASME J. Biomech. Eng.* 117 (1995) 136–145.
48. T. Hisada and H. Noguchi, *Principle and Application of Non Linear Finite Element Methods* (Maruzen, Tokyo, Japan, 1995) (in Japanese).
49. M. E. Zobitz, Z. Luo and K. An, Determination of the compressive material properties of the supraspinatus tendon, *ASME J. Biomech. Eng.* 123 (2001) 47–51.
50. D. Bogen, Strain energy description of biological swelling I single fluid compartment models, *ASME J. Biomech. Eng.* 109 (1987) 252–256.
51. Y. Fung, S. Liu and J. Zhou, Remodeling of the constitutive equation while a blood vessel remodels itself under stress, *ASME J. Biomech. Eng.* 115 (1993) 453–459.
52. Y. Fung, Biorheology of soft tissue, *Biorheology* 10 (1973) 139–155.
53. Y. Ling, Uniaxial true stress-strain after necking, *AMP J. Technol.* 5 (1996) 37–48.
54. H. Demiray, A note of the elasticity of soft biological tissues, *J. Biomech.* 5(3) (1972) 309–311.
55. D. Terzopoulos and K. Fleischer, Deformable models, *The Visual Comput.* 4 (1988) 306–331.
56. S. Cotin, H. Delingette and N. Ayache, Real-time volumetric deformable models for surgical simulation using finite elements and condensation, in *Proc. Eurograph. 96* (Springer–Verlag, New York, 1996), pp. 57–66.

57. G. Szekely, C. Brechbuehler, R. Hutter, A. Rhomberg, N. Ironmonger and P. Schmid, Modeling of soft tissue deformation for laparoscopic surgery simulation, *Med. Image Anal.* 4 (2000) 57–66.
58. S. K. Kyriacou and D. Davatzikos, A biomechanical model of soft tissue deformation with applications to non-rigid registration of brain images with tumor pathology, in *Proc. MICCAI 98, LNCS 1496* (Springer–Verlag, New York, 1998), pp. 531–538.
59. J. B. A. Mainz and M. A. Viergever, A surgery of medical image registration, *Med. Image Analy.* 2(1) (1998) 1–36.
60. D. J. Hawks, P. J. Ewards, D. Barratt, J. M. Blackall, G. P. Penney and C. Tanner, Measuring and modeling soft tissue deformation for image guided interventions, in *Surgical Simulation and Soft Tissue Modeling, LNCS 2673*, N. Ayache and H. Delingette, eds. (Springer–Verlag, New York, 2003), pp. 1–14.
61. H. F. Reinhart, CT-guided real-time stereotaxy, *Acta Neurochir. Suppl.* 46 (1989) 107–108.
62. D. Aulignac, R. Balaniuk and C. Laugier, A haptic interface for a virtual exam of the human thigh, *Proc. IEEE Int. Conf. Robotics Automat.* (2000), pp. 2452–2456.
63. I. Brouwer, Measuring *in vivo* animal soft tissue properties for haptic modeling in surgical simulation, in *Proc. Med. Meets Virtual Reality* (IOS Press, 2001), pp. 69–74.
64. S. Doko, J. J. LeGrice and B. H. Smaill, A triaxial-measurement shear-test device for soft biological tissues, *J. Biomech. Eng.* 122 (2000) 471–478.
65. A. E. Kerdok, Soft tissue characterization: mechanical property determination from biopsies to whole organs, *Whitaker Foundation Biomedical Research Conference*, 2001.
66. J. G. Snedeker, M. Barbezat, P. Niederer, F. R. Schmidlin and M. Farshad, Strain energy as a rupture criterion for the kidney: Impact tests on porcine organs, finite element simulation, and a baseline comparison between human and porcine tissues, *J. Biomech.* 38 (2005) 993–1001.
67. D. L. Vawter, Y. C. Fung and J. B. West, Constitutive equation of lung tissue elasticity, *ASME J. Biomech. Eng.* 101 (1980) 38–45.
68. Z. Liu and L. Bilston, On the viscoelastic character of liver tissue: Experiments and modeling of linear behavior, *Biorheology* 37(3) (2002) 191–201.
69. Z. Liu and L. Bilston, Large deformation shear properties of liver tissue, *Biorheology* 39(6) (2000) 735–742.
70. D. W. A. Brands, G. W. M. Peters and P. H. M. Bovendeerd, Design and numerical implementation of a 3D nonlinear viscoelastic constitutive model for brain tissue during impact, *J. Biomech.* 37 (2004) 127–134.
71. L. Bilson, Z. Liu and N. Phan-Tien, Large strain behavior of brain tissue in shear — Some experimental data and differential constitutive model, *Biorheology* 38 (2001) 335–345.
72. J. D. Brown, J. Rosen, Y. S. Kim, L. Chang, M. N. Sinanan and B. Hannaford, *In vivo* and *in situ* compressive properties of porcine abdominal soft tissues, in *Proc. Med. Meets Virtual Reality* (IOS Press, 2003), pp. 26–32.
73. A. E. Kerdok, M. P. Ottensmeyer and R. D. Howe, The effects of perfusion on the viscoelastic characteristics of liver, *J. Biomech.* (2005) In Press.
74. C. Chui, E. Kobayashi, X. Chen, T. Hisada and I. Sakuma, Tranversely isotropic properties of porcine liver tissue: Experiments and constitutive modeling, *Med. Biol. Eng. Comput.* 45(1) (2007) 99–106.

CHAPTER 8

ULTRASOUND MEASUREMENT OF SWELLING BEHAVIORS OF ARTICULAR CARTILAGE *IN SITU*

QING WANG and YONG-PING ZHENG*
Department of Health Technology and Informatics
The Hong Kong Polytechnic University
Kowloon, Hong Kong, China
**ypzheng@ieee.org*

1. Introduction

1.1. *Articular cartilage*

Articular cartilage is the thin white layer of soft connective tissue that covers the articulating bony ends in diarthrodial joints, such as the end surfaces of the tibia and femur, and the posterior surface of the patella inside the knee joint. Although articular cartilage is a tiny tissue in the body, it provides joints with excellent lubrication and wearing characteristics, and maintains a smooth efficient force-bearing system. It is hard to imagine how the skeleton to bear the weight of the body and conduct the movement without articular cartilage. It has been found that the exact compositions and structure of articular cartilage depend greatly on anatomy location, depth, and age, as well as the pathological state of the tissue.[1–3] The complex hydrated-charged nature and magic functions of articular cartilage have attracted tremendous research interests.

1.1.1. *Negative charged proteoglycan-collagen matrix*

Chondrocytes, proteoglycans (PGs), collagens and water are the major components of articular cartilage. Therefore, articular cartilage is usually regarded to consist of chondrocytes and extracellular matrix (ECM, 95% of the total wet weight).[1] The ECM is primarily composed of water (75% of wet weight), collagen fibrils (mainly type II) (20%), PGs (5%), and other components, such as enzymes, growth factors, lipids, and adhesives.[1]

PGs and collagens interact with each other to form the porous solid matrix swollen with water. PGs are bio-macromolecules, produced by chondrocytes and secreted into the matrix. A single PG aggregan molecule consists of a protein core to which numerous glycosaminoglycan (GAG) chains are bounded by sugar bonds. The aggregated PGs are strongly electronegative due to the negatively charged groups

SURGICAL
CLINICS OF
NORTH AMERICA

Surg Clin N Am 83 (2003) 1429–1444

Robot-assisted gastric surgery

Makoto Hashizume, MD, PhD, FACS*,
Keizo Sugimachi, MD, PhD, FACS

Graduate School of Medical Sciences, Kyushu University, 3-1-1 Maidashi, Higashi-ku, Fukuoka 812-8582, Japan

Recent technological advancements have led to the rapid development of endoscopic surgery all over the world. Many types of open surgery are now being replaced by endoscopic procedures. A number of patients have now successfully undergone minimally invasive surgery. Minimally invasive surgery provides less postoperative pain, a shorter hospital stay, and a faster recovery after surgery. Endoscopic surgeons still face numerous difficulties in both the movement of the instruments and in obtaining a sufficient operative field, however. Most surgeons now feel a greater amount of stress during endoscopic surgery since minimally invasive surgery has been introduced. This is mainly because of the limitations of using instruments in the abdominal cavity via small holes and the narrow vision of the operative field on the monitor. As a result, the merits of endoscopic surgery for the patients and surgeons remain controversial.

Robotic and computer-assisted systems are now making exceptional progress in the field of minimally invasive cardiac surgery. Two competing systems, namely the da Vinci system by Intuitive Surgical, Inc., Sunnyvale, California, and the ZEUS system by Computer Motion, Inc., Sunnyvale, California have targeted cardiac surgery for their introduction into the surgical field. Cadiere et al [1] reported the use of robotic systems in general surgery cases; however, the efficacy of these procedures has not been demonstrated as dramatically in general surgery as in cardiac surgery.

Robot-assisted gastric surgery is now as feasible in patients with early gastric cancer as open surgery [2]. We herein introduce the indications and techniques for robot-assisted gastric surgery.

* Corresponding author.
E-mail address: mhashi@dem.med.kyushu-u.ac.jp (M. Hashizume).

doi:10.1016/S0039-6109(03)00158-0